

# Strong Light–Matter Interactions in Au Plasmonic Nanoantennas Coupled with Prussian Blue Catalyst on BiVO<sub>4</sub> for Photoelectrochemical Water Splitting

T. Gamze Ulusoy Ghobadi,<sup>[a]</sup> Amir Ghobadi,<sup>[b, c]</sup> Mahmut Can Soydan,<sup>[b, c]</sup>  
Mahsa Barzgar Vishlaghi,<sup>[d, e]</sup> Sarp Kaya,<sup>[d, e]</sup> Ferdi Karadas,<sup>\*,[a, f]</sup> and Ekmel Ozbay<sup>\*,[a, b, c, g]</sup>

A facial and large-scale compatible fabrication route is established, affording a high-performance heterogeneous plasmonic-based photoelectrode for water oxidation that incorporates a CoFe–Prussian blue analog (PBA) structure as the water oxidation catalytic center. For this purpose, an angled deposition of gold (Au) was used to selectively coat the tips of the bismuth vanadate (BiVO<sub>4</sub>) nanostructures, yielding Au-capped BiVO<sub>4</sub> (Au-BiVO<sub>4</sub>). The formation of multiple size/dimension Au capping islands provides strong light–matter interactions at nanoscale dimensions. These plasmonic particles not only enhance light absorption in the bulk BiVO<sub>4</sub> (through the excitation of Fabry–Perot (FP) modes) but also contribute to photo-

current generation through the injection of sub-band-gap hot electrons. To substantiate the activity of the photoanodes, the interfacial electron dynamics are significantly improved by using a PBA water oxidation catalyst (WOC) resulting in an Au-BiVO<sub>4</sub>/PBA assembly. At 1.23 V (vs. RHE), the photocurrent value for a bare BiVO<sub>4</sub> photoanode was obtained as 190  $\mu\text{A cm}^{-2}$ , whereas it was boosted to 295  $\mu\text{A cm}^{-2}$  and 1800  $\mu\text{A cm}^{-2}$  for Au-BiVO<sub>4</sub> and Au-BiVO<sub>4</sub>/PBA, respectively. Our results suggest that this simple and facial synthetic approach paves the way for plasmonic-based solar water splitting, in which a variety of common metals and semiconductors can be employed in conjunction with catalyst designs.

## Introduction

Conversion of sunlight into electricity and chemical energy are the major paths to produce green energy. Unlike semiconductors, which only harvest photon energies above their band gap, nanometals exhibit resonant light absorption in the whole electromagnetic spectrum, through the excitation of localized surface plasmon resonances (LSPRs) and inter-band transitions. Thus, plasmonic photoelectrochemical water splitting (PEC-WS) offers a promising approach to convert sunlight into chemical energy, which has recently received intense research.<sup>[1–7]</sup> Plasmonic nanometals can contribute to the semiconductor activity enhancement through two main pathways; i) radiative (scattering, optical near field coupling) and ii) non-

radiative energy transfer (hot electron injection, plasmon resonant energy transfer).<sup>[1]</sup> In the former mechanism, the plasmonic nanoantenna can improve light absorption for above-band-gap photons, whereas the latter can provide sub-band-gap light harvesting.

Although one of the most successful semiconductors—for plasmonic PEC-WS—is titanium dioxide (TiO<sub>2</sub>), mainly owing to its chemical stability, earth abundance, and cost effectiveness,<sup>[8–16]</sup> however, it suffers from a poor absorption response that only covers the ultraviolet (UV) portion of the solar spectrum. Therefore, in recent years, extensive attempts have been made for the design and realization of plasmonic coupled low

[a] T. G. U. Ghobadi, Prof. F. Karadas, Prof. E. Ozbay  
UNAM—National Nanotechnology Research Center  
Institute of Materials Science and Nanotechnology  
Bilkent University  
6800 Ankara (Turkey)

[b] A. Ghobadi, M. C. Soydan, Prof. E. Ozbay  
Department of Electrical and Electronics Engineering  
Bilkent University  
06800 Ankara (Turkey)

[c] A. Ghobadi, M. C. Soydan, Prof. E. Ozbay  
NANOTAM—Nanotechnology Research Center  
Bilkent University  
06800 Ankara (Turkey)

[d] M. B. Vishlaghi, Prof. S. Kaya  
Chemistry Department  
Koc University  
Istanbul 34450 (Turkey)

[e] M. B. Vishlaghi, Prof. S. Kaya  
TUPRAS Energy Center (KUTEM)  
Koc University  
Istanbul 34450 (Turkey)

[f] Prof. F. Karadas  
Department of Chemistry  
Faculty of Science  
Bilkent University  
06800 Ankara (Turkey)  
E-mail: karadas@fen.bilkent.edu.tr

[g] Prof. E. Ozbay  
Department of Physics  
Faculty of Science  
Bilkent University  
06800 Ankara (Turkey)  
E-mail: ozbay@bilkent.edu.tr

Supporting Information and the ORCID identification number(s) for the author(s) of this article can be found under:  
<https://doi.org/10.1002/cssc.202000294>.

band gap metal oxides for driving water oxidation and reduction reactions.<sup>[17–37]</sup> By decorating plasmonic deep sub-wavelength nanoparticles on a semiconductor, near field effects<sup>[19,32,34]</sup> and hot electron injection<sup>[12,34]</sup> can simultaneously contribute to the overall activity of the cell. Strong light–matter interactions, in the plasmonic–semiconductor interface, can trigger the formation of intense localized fields.<sup>[38]</sup> These confined fields increase the density of photogenerated carriers in the vicinity of the surface, and facilitate the charge separation.<sup>[39,40]</sup> However, larger noble metal particles cannot support LSPRs and have a negligible hot electron injection yield. In this platform, these particles act as a mirror that reflects/scatters light. The formation of Fabry–Perot (FP) resonance modes in the metal–semiconductor nanocavity is the main mechanism in these architectures to harvest solar irradiation. Some recent works have proposed innovative hybrid schemes that take advantage of using both FP resonances (supported by the Au reflector in a nanocavity) and LSPRs (through the use of plasmonic nanoparticles) to achieve the high-performance photoanode in PEC-WS systems.<sup>[35,36]</sup>

Besides the superior absorption characteristics of these plasmonic-narrow band gap semiconductor designs, their electrical performance is also a prominent factor. The main bottlenecks of low band gap semiconductors (compared with wide band gap ones) are their shorter diffusion length and higher recombination rate. Therefore, just a portion of carriers in the vicinity of their surface can participate in a water oxidation reaction. This drawback can be intensified in the presence of plasmonic nanometals. These metallic nanoparticles act as an electron trapping center, which captures the photocarriers and hampers their collection efficiency. That is why an optimum metal loading is required to make the necessary trade-off for performance improvement.<sup>[40–42]</sup> Another approach could be the use of a proper catalyst for the selective isolation of photogenerated carriers to enhance their lifetime.<sup>[33,36]</sup> Therefore, in an ideal scheme, a low band gap semiconductor loaded with a plasmonic-catalyst heterostructure with selective decoration can reveal superior opto-electronic and catalytic properties. Moreover, the simultaneous formation of small and large particles could excite both FP and LSPR modes to achieve both semiconductor light absorption enhancement and plasmonic hot electron injection. In recent studies,<sup>[13,43,44]</sup> we developed a facial route based on oblique angle deposition to synthesize plasmonic nanostructures on a large scale. Moreover, we demonstrated that as a result of the cyanide chemistry, so-called CoFe-Prussian blue analog (PBA) is a strong and robust water oxidation catalyst (WOC), when connected to an organic chromophore.<sup>[45,46]</sup> Inspired by these studies, herein, we adopt an extendable platform for the realization of a catalyst-plasmonic architecture to improve the performance of semiconductor photoanodes with a facial and large-scale compatible design in PEC-WS.

For this purpose, bismuth vanadate ( $\text{BiVO}_4$ ) nanostructures are capped with Au particles by using a shadowing effect of oblique angle deposition. In this method, the dimension and shape of Au capping units are defined by the shape of  $\text{BiVO}_4$  and, therefore, it leads to the formation of multiple sized/

shaped particles. The larger particles enhance light absorption within the semiconductor bulk, through light scattering and FP resonance modes. The small ones provide sub-band-gap absorption and contribute to the photocurrent by LSPR-induced hot electron injection. Finally, to optimize the electron dynamics, PBA, as a WOC, is decorated on the surface of the photoanode. As a result of these modifications, the photocurrent value at 1.23 V (vs. reversible hydrogen electrode, RHE) is enhanced by an order of magnitude compared with that of bare  $\text{BiVO}_4$  (from  $190 \mu\text{A cm}^{-2}$  to  $1800 \mu\text{A cm}^{-2}$ ).

## Results and Discussion

For the preparation of a plasmonically modified  $\text{BiVO}_4$  electrode ( $\text{Au-BiVO}_4$ ), an oblique angle physical vapor deposition procedure was adapted to selectively coat Au on the tip of the photoanode, represented schematically in Figure 1a. Oblique deposition, sometimes referred to as glancing angle deposition, is a physical vapor deposition technique that is used to form a nanostructured film with adjustable density and columnar grain growth in the vapor flux direction.<sup>[47]</sup> In this approach, a sample is placed in a position that is oblique to evaporated atoms. When the evaporated flux reaches the substrate, an additional factor is introduced into the growth process, which can result in nanostructures instead of a continuous layer. It is widely accepted that the mechanistic factor controlling the nanostructural evolution of the films is an atomic-scale “shadowing effect”, which prevents the deposition of particles in regions situated behind the initially formed nuclei (i.e., shadowed regions). Inspired by this technique, we have developed the proposed design. In our case, the previously grown nanostructures are exposed into the gold vapor. Owing to the shadowing effect of  $\text{BiVO}_4$  nanostructures, only their tip is coated. The tip size and its direction define the size and shape of the gold caps. As depicted in Figure 1a, the sample is placed on the holder with an incident angle as wide as  $80\text{--}85^\circ$ . As the gold vapor cannot reach the bulk of the  $\text{BiVO}_4$  nanostructure owing to this shadowing effect, only the tips of the photoanodes are coated. From the top view of the SEM images for bare  $\text{BiVO}_4$  and  $\text{Au-BiVO}_4$  (Figure 1b,c), it is clear that the gold capping has not changed the morphology of the bare sample. The magnified image in Figure 1c, inset, clearly reveals the expected formation of Au decoration on the  $\text{BiVO}_4$  photoanode. Further analysis of the photoanodes' morphology and the gold caps can be acquired by cross-sectional SEM images, shown in Figure 1d,e. As labelled in panel d, a thin layer of Au is coated on the tip of  $\text{BiVO}_4$ , in which the shape and size of the Au nanoislands are defined by the morphological character of the  $\text{BiVO}_4$  host and, therefore, an inherent randomness is present in the geometries of Au tips. This can be also seen from elemental energy-dispersive X-ray spectroscopy (EDS) mapping, shown in Figure S1 (in the Supporting Information). We will later discuss that; this randomness will trigger a strong light–matter interaction throughout an ultra-broadband wavelength range, through the excitation of LSPR and FP modes. After the successful fabrication of the plasmonic photoanode, structural characterizations were applied. Raman

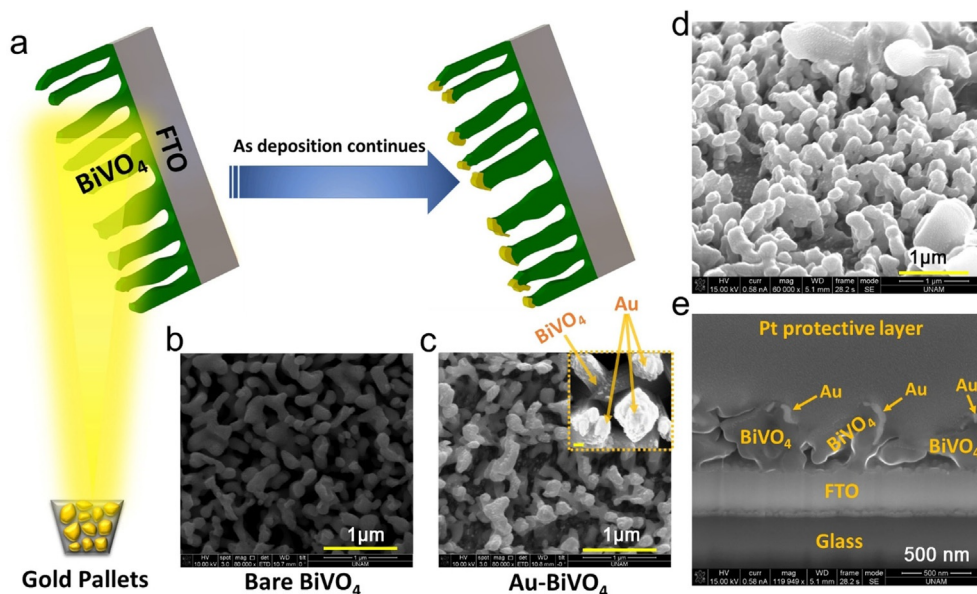


**Figure 1.** (a) Representation of the fabrication route for preparing gold-capped  $\text{BiVO}_4$  photoanodes by using oblique angle physical vapor deposition. The position of electrodes (with an  $80\text{--}85^\circ$  angle) resulted in Au nanoisland formation, yielding the Au- $\text{BiVO}_4$  plasmonic photoanode. A top-view of the SEM images of the (b) bare  $\text{BiVO}_4$  and (c) Au- $\text{BiVO}_4$  photoanodes, scale bar:  $1\ \mu\text{m}$  and the inset shows the high-magnification image of the SEM, scale bar:  $20\ \text{nm}$ . (d) Cross-sectional SEM images of the Au- $\text{BiVO}_4$  photoanode, illustrating the morphology of the nanostructure photoanode. (e) Cross-sectional FIB image of the Au- $\text{BiVO}_4$  sample, showing the formation of multiple sized/shaped Au nano capping islands.

spectroscopy features shown in Figure 2a are in agreement with monoclinic  $\text{BiVO}_4$ .<sup>[48,49]</sup> The most intense Raman band at about  $826\ \text{cm}^{-1}$  is assigned to the symmetric ( $\nu_s$ ) V-O stretching mode ( $A_g$  symmetry), and the weak shoulder at about  $710\ \text{cm}^{-1}$  is assigned to asymmetric ( $\nu_{as}$ ) V-O stretch ( $B_g$  symmetry). The symmetric ( $A_g$ ) and anti-symmetric ( $B_g$ ) bending

modes appear at  $366\ \text{cm}^{-1}$  and about  $325\ \text{cm}^{-1}$ , respectively. The peaks at  $209$  and  $124\ \text{cm}^{-1}$  originate from external modes (rotation/translation). Additional peaks that could originate from  $\text{Bi}_2\text{O}_3$  (at  $315$  and  $448\ \text{cm}^{-1}$ ),  $\text{V}_2\text{O}_5$  (at  $440$  and  $980\ \text{cm}^{-1}$ ), or any other Bi-rich phase were not detected.<sup>[49]</sup> Furthermore, XRD analysis was performed to identify the crystalline structure

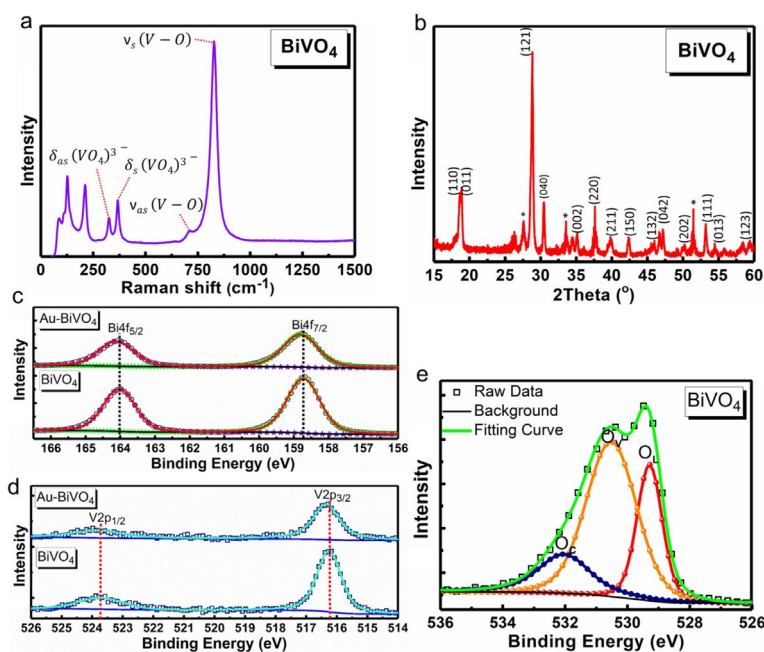


**Figure 2.** (a) Raman spectrum and (b) XRD patterns with diffraction patterns of pristine  $\text{BiVO}_4$  film conforming to its monoclinic phase, “\*” indicates crystal planes of the FTO substrate. High-resolution XPS spectra of (c) Bi 4f and (d) V 2p spectra for the as-prepared  $\text{BiVO}_4$  and Au- $\text{BiVO}_4$  electrodes. (e) The O 1s spectrum of the pristine  $\text{BiVO}_4$  film, which is deconvoluted into three different peaks indicating the presence of three types of oxygen: lattice oxygen ( $\text{O}_l$ ), oxygen vacancy ( $\text{O}_v$ ), and chemisorbed oxygen ( $\text{O}_c$ ).

of the  $\text{BiVO}_4$  sample. The XRD pattern (Figure 2b) clearly reveals that the diffraction peaks of the bare  $\text{BiVO}_4$  sample are in agreement with the standard diffraction patterns of monoclinic  $\text{BiVO}_4$  (JCPDS 01-075-1866) confirmed by the prominent (110) and (011) planes at about the characteristic splitting peak of  $2\theta = 18.5^\circ$ .<sup>[50]</sup> No diffraction peaks from any other impurities are detected. To determine the specific surface composition and chemical state of the  $\text{BiVO}_4$  and  $\text{Au-BiVO}_4$ , XPS measurements were employed. The high-resolution XPS spectra of Bi4f and V2p are shown in Figure 2c,d, respectively. The two strong peaks at 164.03 eV and 158.73 eV with the orbital splitting of 5.3 eV, corresponding to  $\text{Bi}4f_{5/2}$  and  $\text{Bi}4f_{7/2}$ , are the characteristics of  $\text{Bi}^{3+}$  species for the as-prepared  $\text{BiVO}_4$  film.<sup>[51,52]</sup> The 1/2 and 3/2 spin-orbit doublet components of the  $\text{V}^{5+}$  of the same electrode are located at 523.7 eV and 516.25 eV, respectively (see Figure 2d).<sup>[53,54]</sup> After the deposition of Au nanoislands, the V2p and Bi4f peaks are slightly blue shifted ( $\approx 0.1$  eV) compared with the bare  $\text{BiVO}_4$ , suggesting an electron transfer from Au to  $\text{BiVO}_4$ , which could be attributed to the relatively high electronegativity of Au (see Figure 2c,d).<sup>[54–57]</sup> Moreover, the characteristic peaks at 87.18 eV and 83.5 eV in Figure S2 (in the Supporting Information) are ascribed to  $\text{Au}4f_{5/2}$  and  $\text{Au}4f_{7/2}$ , respectively,<sup>[58]</sup> for  $\text{Au-BiVO}_4$ . The XPS measurements are not only used to provide information about the surface composition of the sample, but it can also be employed to study the surface properties of the layer and the electronic band structure of the design. For the investigation of the existence of surface defects, the O1s spectra of the samples were analyzed. The core-level O1s spectrum of as-prepared  $\text{BiVO}_4$  is deconvoluted into three Gaussian peaks, as explained in our previous study.<sup>[59]</sup> The major O1s peak at around 529.30 eV is attributed to the lattice oxygen atoms ( $\text{O}_\text{L}$ ) in the metal oxide. This low-binding peak is attributed to  $\text{O}^{2-}$  coordinated with the  $\text{V}^{5+}$  and  $\text{Bi}^{3+}$  ions in the bulk  $\text{BiVO}_4$ . The other two Gaussian components with center binding energies of 530.53 eV and 532.06 eV are assigned to oxygen vacancies or defects ( $\text{O}_\text{V}$ ) and chemisorbed oxygen species ( $\text{O}_\text{C}$ ), respectively. Owing to water adsorption and dissociation at the surface, hydroxyl groups can be coordinated to the metal ions (M–O bonds) in the oxygen deficient region ( $\text{O}_\text{V}$ ).<sup>[60]</sup> These oxide ions could be described as low-coordinated oxygen ions, O-species, with lower electron densities than the lattice oxygen atoms. The surface dissociated oxygen or OH species can also be loosely attached to the surface ( $\text{O}_\text{C}$ ) such as through dangling oxo-bonds.<sup>[52,55,61–64]</sup> These loosely surface-adsorbed oxygen or OH species increase the hydroxyl concentration on the electrode surface.<sup>[60]</sup> As this graph clearly implies, in the case of bare  $\text{BiVO}_4$ , the nanoporous sample has a relatively large density of the  $\text{O}_\text{V}$  and  $\text{O}_\text{C}$  components. These oxygen defects in the metal oxide surface can trap the charge carriers at the surface and result in interfacial charge recombination as found in previous articles.<sup>[65,66]</sup> A similar profile is detected for  $\text{Au-BiVO}_4$  (see Figure S3 in the Supporting Information), which is expected, considering the fact that the gold capping layer has been physically evaporated onto the surface, rather than being chemically bonded. Overall, the  $\text{BiVO}_4$  photoanode is an oxygen defect rich sample and, therefore, its PEC-

WS performance is poor. The effect of oxygen vacancies on the  $\text{BiVO}_4$  PEC performance is still under debate in the literature. Recent works indicate that oxygen vacancies can have multiple roles on the PEC-WS performance of metal oxides.<sup>[62,67–73]</sup> From the positive side, it is commonly accepted that oxygen vacancies inside the bulk medium improve the free carrier concentration and consequently lead to better charge carrier transport.<sup>[73]</sup> Moreover, some authors have highlighted the electrocatalytic function of these trap states, if they are located on the surface.<sup>[73]</sup> However, it should be noted that not all types of trap states can provide this beneficial impact. Essentially, traps can be categorized into two main groups; 1) shallow traps and 2) deep traps.<sup>[74,75]</sup> Shallow traps that are energetically close to the conduction band of the metal oxide can be excited into the conduction band by thermal activation and, thus, they can improve the overall bulk conductivity. However, electrons or holes in the deep trap states cannot be detrapped, which act as charge recombination centers to reduce the transport efficiency. Moreover, it has been shown that the carriers in deep hole trap states are energetically unable to drive water oxidation.<sup>[72]</sup> Although the above-mentioned discussion implies that trap states could introduce bulk conductivity and surface electro-catalytic performance, they have a major detrimental impact on the interfacial charge transfer where they mediate electron–hole recombination.<sup>[73]</sup> Owing to this trade-off, the density of these oxygen vacancies is a crucial factor to determine their effect on the PEC-WS process. In our sample, the large density of oxygen vacancies can be detected from the XPS measurements. Although this reduces the charge transport resistance within the bulk (as it will be shown from electrochemical impedance spectroscopy (EIS) analysis in the upcoming section), it induces high interfacial charge recombination. Thus, in an ideal scenario, a bulk vacancy level is needed to improve the bulk conductivity, and should suppress the surface trap states to minimize interfacial charge recombination. Gaining an insight into the chemical composition and surface states of the photoanodes, the band alignment between Au and  $\text{BiVO}_4$  should be extracted. For this aim, the energetic level of the valance band maximum (VBM; i.e.,  $E_\text{F} - E_\text{VBM}$ , where the Fermi level energy ( $E_\text{F}$ ) is the zero point) is estimated by using XPS measurements of the valance band (VB) spectra. As illustrated in Figure 3a,b,  $E_\text{VBM} - E_\text{F}$  for  $\text{BiVO}_4$  is found to be 1.52 eV. The VB spectra for the  $\text{Au-BiVO}_4$  sample, however, has a dominant response arising from the top capping of gold. For the sample with Au nanoislands, a 5d-band edge lies at 1.08 eV relative to its  $E_\text{F}$ , whereas the lower energy tail is attributed to 6sp electrons.<sup>[76]</sup> In equilibrium, the Fermi levels of  $\text{BiVO}_4$  and Au will be aligned. Therefore, in this study, the aligned  $E_\text{F}$  of the  $\text{Au-BiVO}_4$  interface is assumed to be located at the original  $E_\text{F}$  of  $\text{BiVO}_4$ . To find the band diagram, we also need to know the band gap of  $\text{BiVO}_4$ . For this purpose, the absorption behaviors of the photoanodes were investigated at a wavelength range of 320–550 nm. As shown in Figure 3c, the UV/Vis spectrum of the  $\text{BiVO}_4$  photoanode has an absorption tail extending up to 490 nm. The optical band gap of  $\text{BiVO}_4$  is estimated from the Tauc plot, as shown in Figure 3c, inset.<sup>[77]</sup> This indirect band gap value of about 2.5 eV is quite well

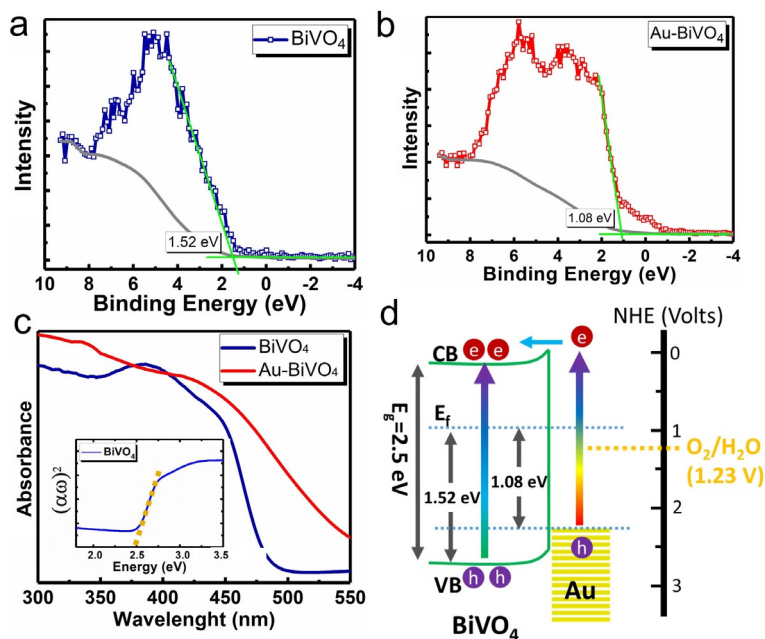


**Figure 3.** XPS valence band spectra of (a) BiVO<sub>4</sub> and (b) Au-BiVO<sub>4</sub>. Green lines show the linear extrapolation of the curves for deriving the valence band edge position of BiVO<sub>4</sub> samples, that is,  $E_f - E_{\text{VBM}}$ . The gray lines also show the background signal. (c) Absorption profiles for both BiVO<sub>4</sub> and Au-BiVO<sub>4</sub> photoanodes in the wavelength range 300–550 nm. The inset shows the Tauc plot used for the estimation of the optical band gap (2.5 eV) of BiVO<sub>4</sub>. (d) Schematic energy band diagram of Au-BiVO<sub>4</sub> showing the band alignments and the involved water oxidation electron transfer processes.

matched with the absorption threshold of BiVO<sub>4</sub>, which is close to the reported value of the monoclinic phase.<sup>[78]</sup> This is in line with Raman spectroscopy and XRD findings, implying the formation of monoclinic phase of BiVO<sub>4</sub>. It should also be noted that, in the same panel, the absorption spectrum for Au-BiVO<sub>4</sub> suggests that the introduction of Au on top of the BiVO<sub>4</sub> nanostructure has improved the light absorption in both the below and above band gap regimes. In the following sections, this will be scrutinized in detail by using numerical simulations. Bringing all of the above results together, the band alignment between different interfaces for the plasmonic Au-BiVO<sub>4</sub> photoanode is schematically illustrated in Figure 3d. According to the extracted energy diagram, the photoexcited hot electrons with energies above the Schottky barrier height will be injected into BiVO<sub>4</sub> and the corresponding hot holes will participate in the water oxidation reaction. Given the aforementioned structural analysis, we further explored the PEC-WS performance of the photoanodes. The PEC water oxidation measurements were performed with a three-electrode cell using the as-prepared BiVO<sub>4</sub> and Au-BiVO<sub>4</sub> as working electrodes (see the cell configuration in Figure 4a). As illustrated in Figure 4b, the linear sweep voltammograms (LSVs) show that Au nanotips in Au-BiVO<sub>4</sub> enhanced the photocurrent response of bare BiVO<sub>4</sub> from 190  $\mu\text{A cm}^{-2}$  to 295  $\mu\text{A cm}^{-2}$  at 1.23 V (vs. RHE). Therefore, the decoration of the photoanode with Au nanoantennas effectively improves the photoactivity of the structure. Moreover, the Au-BiVO<sub>4</sub> photoanode exhibits a plateau at around 0.7 V (vs. RHE), which could be due to the catalytic effect induced by Au nanoislands.<sup>[79,80]</sup> As depicted in Figure 3d, the gold

Fermi level is located between the conduction band of BiVO<sub>4</sub> and the water oxidation level. Thus, the gold nanoislands can act as catalysts for the selective transfer of photogenerated holes to the electrolyte, thereby reducing the recombination rate and improving the interfacial kinetics. The cathodic shift in the onset overpotential under light illumination also supports this thesis. The photogenerated holes in the BiVO<sub>4</sub> valence band and hot holes formed in the gold nanounits are, thus, responsible for this photocurrent enhancement. As the applied bias increases, the electron dynamics are improved and the current increases exponentially, similar to that of the bare BiVO<sub>4</sub> LSV profile. Overall, gold nanoislands introduce three main functions: i) enhancing the light absorption in BiVO<sub>4</sub> photoanode, ii) generating hot holes for the direct oxidation of water, and iii) acting as a co-catalyst that mediates the electron transfer from BiVO<sub>4</sub> valence band to the electrolyte. To test the long-term stability of the photoanode, transient photocurrent measurements by the chronoamperometry (CA) technique were conducted on Au-BiVO<sub>4</sub> for a duration of 60 min at 1.23 V (vs. RHE). As seen in Figure 4c, bare and plasmonic samples have stable operation over this period of time, which confirms the stability of both electrodes. From the previous section's findings, the as-prepared BiVO<sub>4</sub> samples are oxygen deficient and so these oxygen vacancy levels act as shallow/

deep trap states, which capture the photogenerated carriers. Although some reports claim the positive impact of these surface traps in the water oxidation reaction, their existence in the bulk or vicinity of the surface may hamper charge transport and increase their recombination probability.<sup>[81]</sup> Here, this is likely the main reason behind the poor photoactivity of the bare BiVO<sub>4</sub> photoanode. Open circuit voltage decay (OCVD) measurements can provide us with a qualitative comparison of this issue. In this technique, the sample is left upon light illumination, and then the voltage decay profile is probed after light cut-off. The difference between open circuit potential in dark and light conditions is called photovoltage and it is a direct measure of photoactivity of the photoanode. As Figure 4d implies, the photovoltage is slightly larger for the Au-BiVO<sub>4</sub> sample ( $\approx 0.22$  V), compared with that of the bare sample ( $\approx 0.20$  V). This enhancement originates from the stronger light-matter interactions in the plasmonic sample, which lead to the larger density of photogenerated carriers. A more visible difference can be found in the temporal decay profiles of OCVDs. The decay traces for both samples was fitted with a biexponential function having time constants of  $\tau_1$  and  $\tau_2$ .<sup>[82,83]</sup> These constants for the bare sample were 2.7 s and 92.7 s, whereas those for the plasmonic photoanode are 1.9 s and 44.6 s. The shorter lifetime could be attributed to band-to-band recombination as similar constants were obtained for both samples. The origin of the longer component is, however, different. For the bare sample, there is a single semiconductor layer and no charge separation mechanism is involved, which implies that the prolonged decay profile is due to the exis-

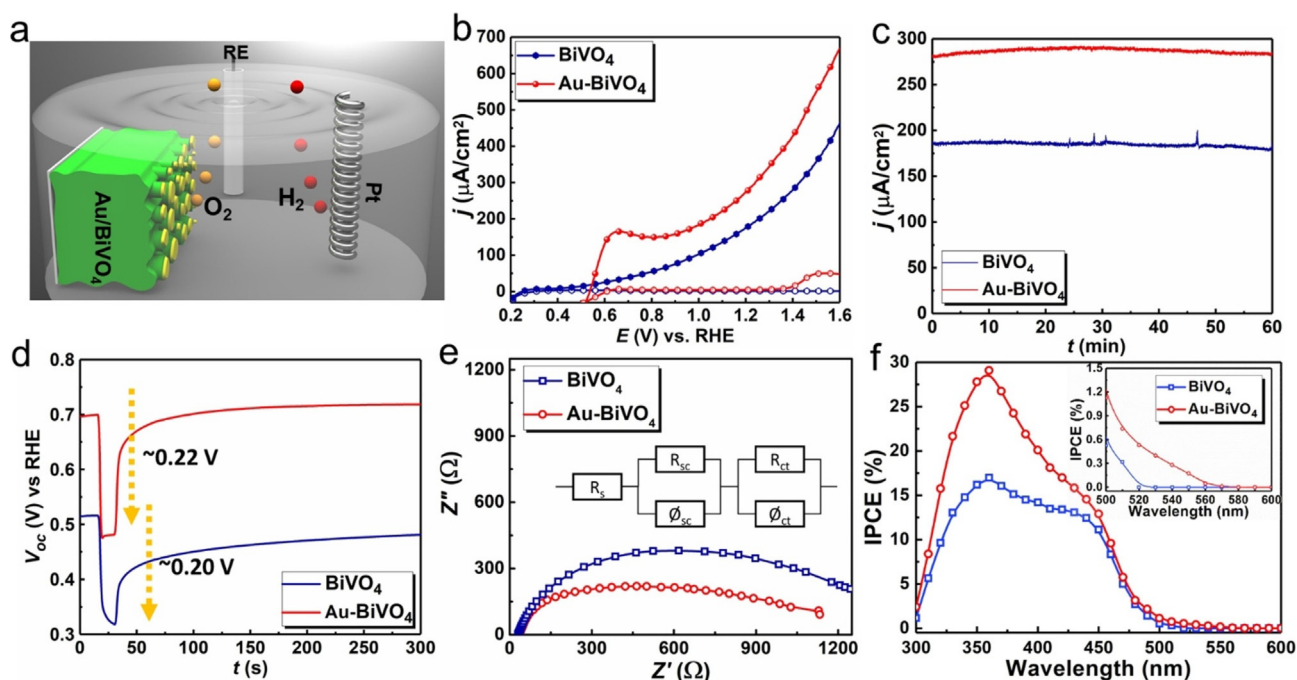


**Figure 4.** (a) Illustrative representations of a 3D schematic of the PEC-WS system consisting of a Au-BiVO<sub>4</sub>-coated FTO electrode (1 cm<sup>2</sup>), as a working electrode. (b) LSV measurements, *j*-*V* curves, of the working electrodes under light illumination (solid symbols), under dark conditions (empty symbols) with a white-light source. Anodic scan rate: 50 mV s<sup>-1</sup>, electrolyte: N<sub>2</sub>-saturated 0.1 M PBS pH 7, light intensity: 100 mW cm<sup>-2</sup>. (c) Chronoamperogram for 1 h of illumination at 1.23 V (vs. RHE) bias. (d) OCVD measurement as a function of time for a duration of 300 s. (e) EIS Nyquist plots at a bias of 1.23 V (vs. RHE) in the frequency range 100 kHz to 0.1 Hz under solar irradiation. The inset shows the circuit model used for fitting. (f) IPCE spectra of the PECs with a 1.23 V (vs. RHE) external bias. The wavelength was scanned from 300 to 600 nm with a step size of 10 nm.

tence of bulk and surface traps. The shallow and deep trap sites capture the carriers and thereby prolong their recombination times. On the other hand, in the plasmonic Au-BiVO<sub>4</sub> sample, the gold particles mediate the recombination between electrons and holes, facilitating their recombination. This claim can be further confirmed by electrochemical impedance spectroscopy (EIS). From the EIS profiles, shown in Figure 4e, the radius of the impedance circle is reduced upon Au plasmonic sensitization. The obtained profiles are fitted to the circuit model shown in the inset of Figure 4e. In this model,  $R_s$  represents the series resistance of the cell (including the fluorine-doped tin oxide, FTO, electrolyte layers),  $R_{ct}$  corresponds to the charge transfer resistance in the semiconductor/electrolyte interface, and  $R_{sc}$  models the resistance within the semiconductor bulk. Moreover, a constant phase element ( $\emptyset$ ) is employed to model the imperfect capacitance because a pure capacitance is an inaccurate choice for describing the semiconductor/electrolyte solution in an actual electrochemical process. The fitting results of the data is summarized in Table S1 (in the Supporting Information). According to these fittings, the most notable change in the resistance values relates to the  $R_{ct}$ , which is expected as our modification is in the semiconductors' surface. The addition of gold nanotips reduces the  $R_{ct}$  from 1280.1  $\Omega$  to 873.6  $\Omega$ , compared with the bare sample. This is in line with the XPS and OCVD findings. Thus, the gold nanoislands act as a catalyst layer and reduce the interfacial charge transfer resistance, a feature that has previously been observed in the LSV profiles as well. Therefore, the Au cap not

only substantiates the optical response of the photoanode, but also improves the electron dynamics. Direct evidence for this claim can be acquired by the assessment of the incident photon-to-current conversion efficiency (IPCE) of the photoanodes. Figure 4f shows the IPCE profiles for bare BiVO<sub>4</sub> and Au-BiVO<sub>4</sub> photoanodes at an applied bias of 1.23 V (vs. RHE). As revealed in this figure, the above-band-gap IPCE values ( $\lambda < 520$  nm) have been enhanced for the plasmonic sample, which is mainly due to the strengthening of the light-matter interactions in the formed metal-semiconductor nanocavities. Moreover, sub-band-gap IPCE values are also present for the Au-BiVO<sub>4</sub> photoanodes, as depicted in the inset. This data confirms the existence of hot electron injection from optically excited gold islands into the BiVO<sub>4</sub> semiconductor. Therefore, the Au capping not only improves the optical and electrical response of the semiconductor as a photoanode, but also acts as a secondary source for photocurrent generation by the injection of hot electrons.

To gain an insight into the impact of Au nanoislands in the optical absorption of the BiVO<sub>4</sub> photoanode, numerical simulations were carried out by using a commercial finite-difference time-domain (FDTD) software package (Lumerical FDTD Solutions).<sup>[84]</sup> The FDTD is a state-of-the-art method for solving Maxwell's equations in complex designs. Being a direct time and space solution, it is a useful method to solve problems related to electromagnetics and photonics. FDTD also offers the frequency solution by utilizing the Fourier transforms, therefore a vast variety of quantities including the complex Poynt-

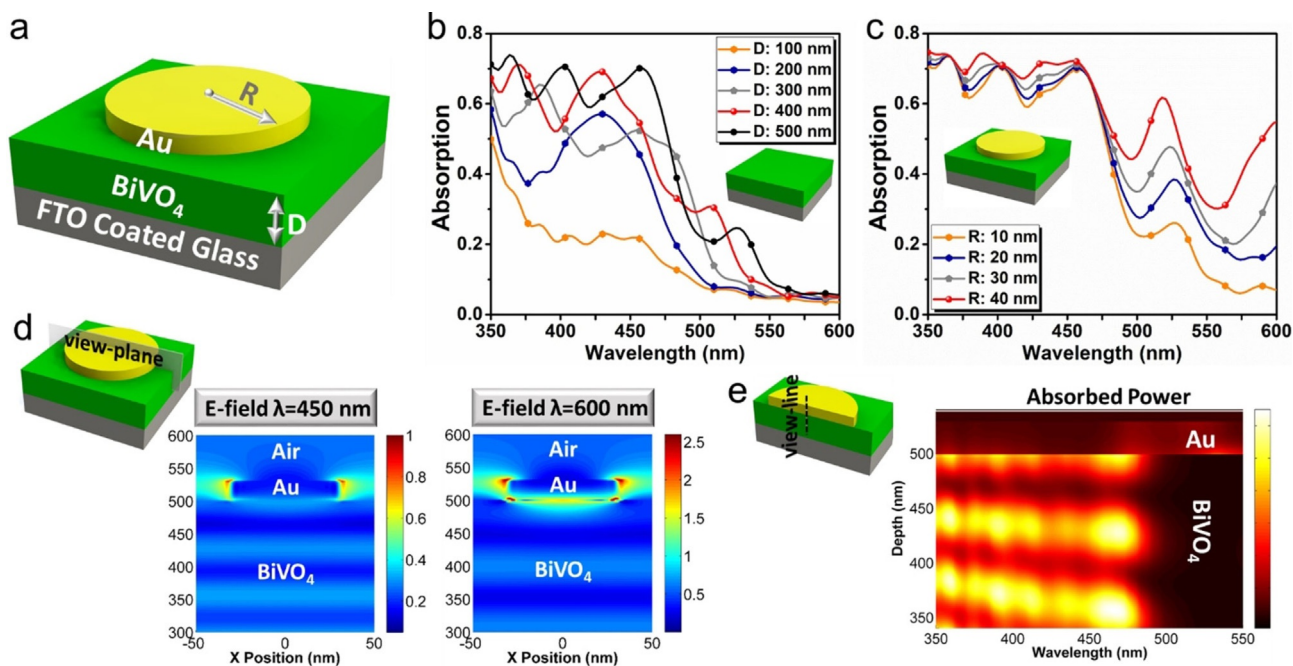


**Figure 5.** (a) The simulation unit cell. The normalized absorption as a function of (b)  $\text{BiVO}_4$  length ( $D$ ) and (c) Au capping radius ( $R$ ). (d) The E-field distribution across the design at 450 nm where  $\text{BiVO}_4$  is optically absorptive, and 600 nm, in which  $\text{BiVO}_4$  is transparent to incoming photons. (e) The absorbed power profile across the view line as a function of incoming wavelength.

ing vector, transmission, and reflection of incident light can be calculated. For this aim, three-dimensional (3D) simulations were employed. A plane-wave excitation in the desired wavelength range (350–600 nm) was employed. The boundary conditions in the lateral directions ( $x$  and  $y$ ) are set as periodic whereas a perfectly matched layer (PML) is assigned for the  $z$  direction. Two monitors were placed to collect the reflected ( $R$ ) and transmitted ( $T$ ) lights. The reflection monitor is placed above the plane-wave and the transmission monitor is placed in the bottom side of the unit cell. The absorbed ( $A$ ) data was calculated by using the following formula  $A = 1 - R - T$ . As explained, in this simulation, we suppose the structure is periodic with a unit cell shown in Figure 5a. Although this assumption is not realistic (looking at the SEM images of the samples), it provides us with an overall understanding of the effect of different geometries on the device optical response. As the initial step, the absorption profile of a simple planar  $\text{BiVO}_4$  is studied. As deduced from Figure 5b, increasing the thickness of the active semiconductor layer improves the absorption property of the design. However, owing to the surface reflection and weak extinction coefficient of the material in longer wavelengths (which leads to light transmission through the layer), the absorption reaches a saturation level far from the unity ideal absorption. It should be noted that the existence of ripples in the absorption spectrum arises from the multiple reflection/transmission in different interfaces. Introducing a top resonant nano gold disc, however, substantiates the response. The gold layer thickness is chosen as 30 nm, which is obtained also from the experimental data (SEM images in Figure 1e). This value has been chosen considering the skin depth of the gold layer (which is around 4 nm with 500 nm wavelength). Thick-

nesses above this depth will have a minor impact on the absorption response of the structure. The absorption enhancement is more pronounced with longer wavelengths (near band edge absorption), where the inherent extinction of the layer is weak, see Figure 5c. Moving from  $R = 10$  nm to  $R = 40$  nm, with the periodicity of the unit cell of 100 nm, the absorption amplitude is increased. To address the mechanisms responsible for this improvement, the electric field (E-field) distribution is probed across the different layers, as schematically illustrated in Figure 5d. At  $\lambda = 450$  nm, where the  $\text{BiVO}_4$  is optically active, the field profile shows the formation of FP resonances within the  $\text{BiVO}_4$ . In addition, a dipole-like field distribution is seen at the location of the Au disc, which likely stems from the excitation of LSPRs in the Au- $\text{BiVO}_4$  interface. At a wavelength of 600 nm, in which the  $\text{BiVO}_4$  is optically transparent, the same mechanisms are present, but different from a shorter wavelength response, a hot spot is created just below the Au nanounit. This strongly localized field triggers the excitation of hot electrons within the gold resonator and the generated hot electrons are injected into the semiconductor layer. Consequently, charge separation is achieved, and hot holes participate in a water oxidation reaction. To verify these estimations, the absorbed power has been calculated along an observation line, as shown in Figure 5e. As implied by this panel, the absorption for the above-band-gap photons occurs dominantly inside the  $\text{BiVO}_4$  layer, whereas the gold nanounit harvests incoming light in the longer wavelength ranges. All of the above-mentioned results prove the superior optical response of the Au- $\text{BiVO}_4$  sample. However, the  $\text{BiVO}_4$  suffers from a large density of oxygen vacancies, which inhibit carrier transportation and diminish the overall photoactivity of the layer.

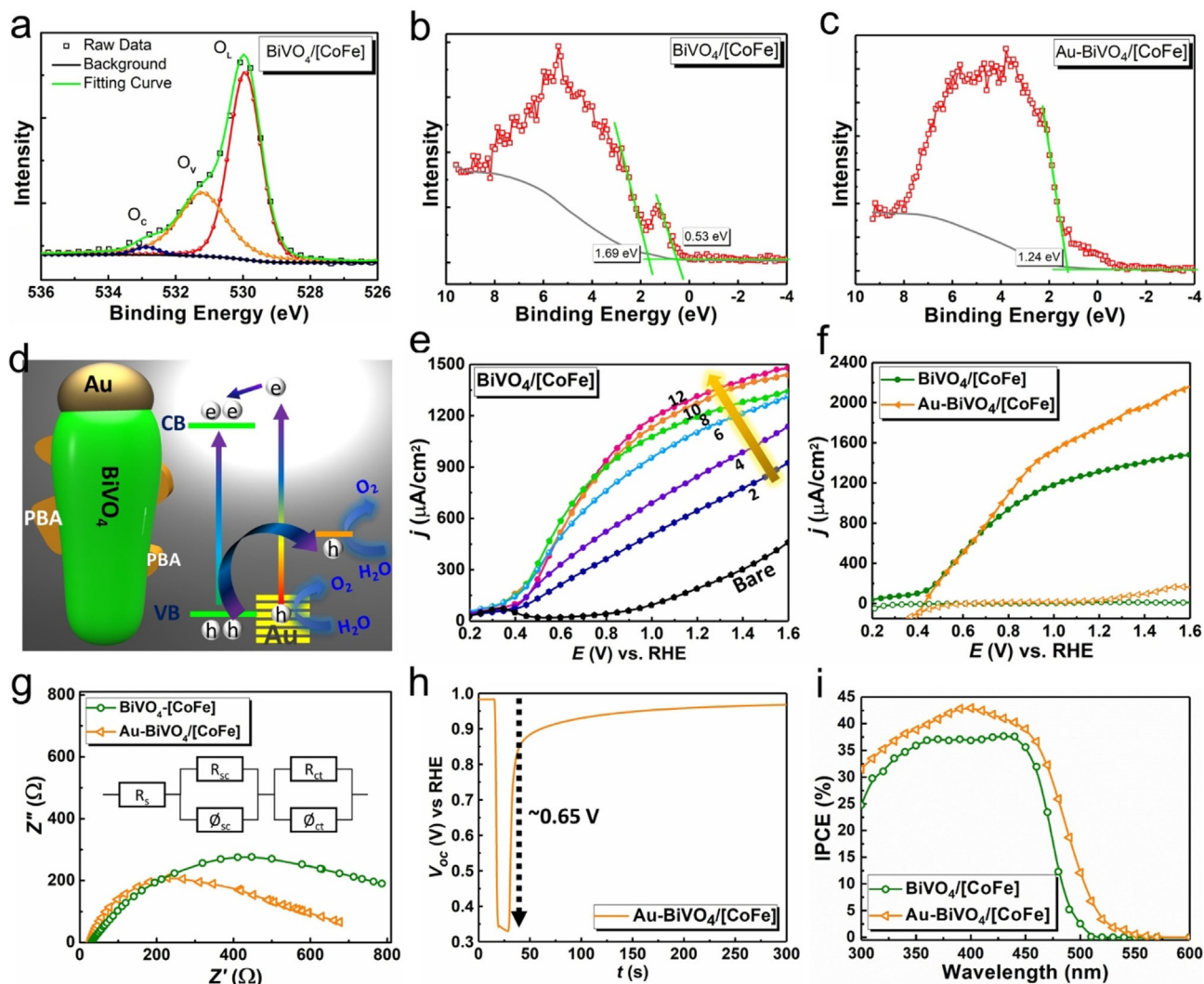


**Figure 6.** High-resolution XPS spectra of (a) O 2p, (b) VB spectra for (BiVO<sub>4</sub>/[CoFe]), and (c) VB spectra for Au-BiVO<sub>4</sub>/[CoFe]. (d) Illustrative representations of the Prussian blue-modified Au-BiVO<sub>4</sub>-coated FTO electrode (1 cm<sup>2</sup>), as a working electrode for the photoelectrochemical water oxidation process. (e) LSV measurements under light illumination,  $j$ - $V$  curves, of the bare BiVO<sub>4</sub> and 2–12 times CoFe-PBA-modified BiVO<sub>4</sub> electrodes. (f) LSV curves for BiVO<sub>4</sub>/[CoFe] and Au-BiVO<sub>4</sub>/[CoFe] under light illumination (solid symbols), and dark conditions (empty symbols) with a white-light source. Anodic scan rate: 50 mV s<sup>-1</sup>, electrolyte: N<sub>2</sub>-saturated 0.1 M PBS pH 7, light intensity: 100 mW cm<sup>-2</sup>. (g) EIS Nyquist plots at a bias of 0.8 V (vs. RHE) in the frequency range 100 kHz to 0.1 Hz under solar irradiation for both electrodes. The inset shows the circuit model. (h) OCVD temporal response throughout a 300 s duration. (i) IPCE spectra of the photoanodes with a 1.23 V (vs. RHE) external bias. The wavelength was scanned from 300 to 600 nm with a step size of 10 nm.

To expedite the electron dynamics in the photoanode/electrolyte interface, a WOC could be employed. Recently, many groups have explored the integration of a Prussian blue assembly with semiconductor and molecular chromophores.<sup>[46, 85, 86]</sup> Overall, it was demonstrated that the addition of CoFe-PBA as a WOC can significantly improve the carrier dynamics of the electrode, by mediating the water oxidation reaction. To understand the impact of this WOC on the surface properties of BiVO<sub>4</sub>, XPS analysis was employed. Although the Bi 4f and V 2p spectra were similar to those of bare the BiVO<sub>4</sub> sample, the O 1s profile was significantly altered. Based on the fitting results in Figure 6a, the ratio of O<sub>V</sub>/O<sub>L</sub> was reduced, compared with that of bare BiVO<sub>4</sub>. Thus, PBA was dominantly attached into the oxygen vacancy positions and effectively passivated the surface traps. This, in turn, leads to an enhancement in the

carrier concentration and the conductivity of the sample. This superior impact can be confirmed by elucidating the VB XPS spectra of the BiVO<sub>4</sub>/[CoFe] and Au-BiVO<sub>4</sub>/[CoFe] photoanodes. For BiVO<sub>4</sub>/[CoFe],  $E_{\text{VBM}} - E_{\text{f}}$  is found to be 1.69 eV, which is increased by 0.17 eV, compared with that of bare BiVO<sub>4</sub>. The shifting of the Fermi level toward the conduction band (CB) originates from the enhancement in the carrier concentration of the BiVO<sub>4</sub> photoanode. Moreover, another signal is in the lower binding energies, which we can assign to the energetic location of CoFe-PBA with an energetic position of 0.53 eV (Figure 6b). The difference in the Au and equilibrium Fermi level of the Au-BiVO<sub>4</sub>/[CoFe] is also found to be 1.24 eV, as shown in Figure 6c. Based on these findings, the Au Fermi level is located at 0.45 eV (1.69–1.24 eV) above the BiVO<sub>4</sub> VBM, expectedly similar to the band alignment in Au-BiVO<sub>4</sub>. The

CoFe-PBA energetic location is 1.16 eV above the BiVO<sub>4</sub> VBM. All these numbers and band positions have been schematically depicted in Figure S4 (in the Supporting Information). According to the extracted energy diagram summarized in Figure 6d, proper alignment is achieved between the BiVO<sub>4</sub> VB and Au Fermi level as well as the CoFe-PBA water oxidation level. Upon light illumination, the photons with energies above the optical band gap excite the electrons from the valance to the conduction band of BiVO<sub>4</sub>. The photoinduced holes move into catalytic sites and participate in a water oxidation reaction. On the other hand, light absorption in the nano Au unit leads to the generation of hot electrons (with sub-band-gap energies). The generated hot electrons, capable of passing the Schottky barrier, are injected into the semiconductor and the remaining hot holes are able to oxidize water. It is noteworthy that in achieving an excellent interfacial carrier dynamic, the loading of the catalyst should be optimized as well. Considering the insulating nature of the catalyst layers, making them too thick will reduce the activity of the overall system. Therefore, in optimum conditions, the catalyst should terminate all trap states, without further unnecessary growth. This can be deduced from Figure 6e, as the sequential dip-coating increases, the photocurrent increases to a point where it is almost saturated. From that point, the photocurrent value in the lower applied biases (where the bias is not enough to trigger the passage of electron through the insulator layer) starts to decline and so the optimum number of dip coating cycles is defined as ten cycles. As a next step, a gold capping layer is introduced to the PBA thickness optimized sample. The Au-BiVO<sub>4</sub>/[CoFe] plasmonic photoanode was fabricated by using the same oblique angle deposition. The LSV profiles have been compared for BiVO<sub>4</sub>/[CoFe] and Au-BiVO<sub>4</sub>/[CoFe] photoanodes in Figure 6f. As shown in this panel, the introduction of gold capping has further substantiated the performance of the catalyst-loaded sample. At 1.23 V (vs. RHE), the photocurrent is raised from 1330 μA cm<sup>-2</sup> (for BiVO<sub>4</sub>/[CoFe]) to a value as high as 1800 μA cm<sup>-2</sup> (for Au-BiVO<sub>4</sub>/[CoFe]). Compared with the bare BiVO<sub>4</sub>, where the photocurrent was determined as 190 μA cm<sup>-2</sup>, the proper use of catalyst-plasmonic combination has improved the activity of photoanode by six-fold. This prominent enhancement is essentially caused by facilitating the electron dynamics via the PBA catalyst. EIS findings demonstrate that the charge transfer resistance (which corresponds to the semi-circle radius) is effectively reduced by CoFe-PBA and a substantial decrease was attained through plasmonic integration, see Figure 6g. The same circuit model has been employed to find the charge transfer resistances. The fitted values are summarized in Table S1 (in the Supporting Information). Based on these results, the  $R_{CT}$  is further decreased to 691.2 Ω and 553.8 Ω for the BiVO<sub>4</sub>/[CoFe] and Au-BiVO<sub>4</sub>/[CoFe] photoanodes, respectively. Moreover, the OCVD reveals a photovoltage of 0.65 V for BiVO<sub>4</sub>/[CoFe], which is significantly larger than that of the bare BiVO<sub>4</sub> sample with much faster photovoltage decay (Figure 4d), as shown in Figure 6h. This essentially originates from the photogeneration of a larger density of electrons upon excitation and could be attributed to the passivation of surface traps through WOC, as expected by the

XPS results. The decay time constants for this sample are found to be 2.4 s and 61.3 s, which are slightly larger than those of the Au-BiVO<sub>4</sub> photoanode. This enhanced lifetime is due to the selective separation of carriers through the extraction of photogenerated holes in the semiconductor-WOC interface. Finally, IPCE measurements were carried out to understand the contribution of the near field effects and hot electron injection. As shown in Figure 6i, the photoconversion efficiency of the design has been improved in all the incident wavelengths, with a maximum as high as 37% for BiVO<sub>4</sub>/[CoFe], and 43% for the Au-BiVO<sub>4</sub>/[CoFe] sample. In comparing the obtained results for the pristine BiVO<sub>4</sub> photoanode, the introduction of PBA WOC improves the IPCE for all incoming photon energies. This essentially stems from the efficient interfacial electron dynamics through the WOC. For the Au-BiVO<sub>4</sub>/[CoFe], the coupling of light into FP and LSPR modes has intensified the light absorption and consequently the number of photogenerated carriers. By means of the WOC, these excess photogenerated electrons participate in a water oxidation reaction and the IPCE increases. Moreover, the enhancement is stronger in longer ranges, that is, near band gap photons. This is because of the weak absorption response of BiVO<sub>4</sub> for the near band edge photons and, therefore, the proposed trapping scheme is more efficient in this spectral range. The enhancement in the  $\lambda > 520$  nm spectral range is essentially caused by hot electron injection from the plasmonic nanoislands. All the above-mentioned results have important implications for developing feasible plasmonic-catalysts on the semiconductor for solar water splitting. Finally, it should be noted that the theoretical limit of BiVO<sub>4</sub> is around 7.5 mA cm<sup>-2</sup> at 1.23 V (vs. RHE).<sup>[87]</sup> Although many studies have tried to reach this limit, the reported maximum current densities are 6.1 mA cm<sup>-2</sup> at 1.23 V (vs. RHE)<sup>[88]</sup> and 6.7 mA cm<sup>-2</sup> at 1.23 V (vs. RHE).<sup>[89]</sup> This proof-of-concept study provides an alternative approach to enhance the PEC performance of a semiconductor layer through the combinational use of a WOC and plasmonic particles with proper arrangement. The proposed fabrication route can be easily extended into other plasmonic hetero-junction designs with no material restrictions. Thus, it can be used in a wide variety of materials for future performance-enhanced PEC-WS cells.

## Conclusions

In this work, we have developed a facial, and large-scale compatible approach to fabricate plasmonic photoanodes for hot electron-driven water oxidation utilizing a cyanide-based catalyst assembly. First, the proposed structure, Au-BiVO<sub>4</sub> shows a superior optical response with a broadband absorption in the visible part of the spectrum. The multiple sized/shaped nature of the formed Au nanoislands triggers the excitation of FP trapping modes and LSPRs. FP modes are effective trapping schemes at  $\lambda < 520$  nm (above-band-gap photons), whereas LSPR reveals their contribution for sub-band-gap photons ( $\lambda > 520$  nm) through hot electron injection. Then, the superior absorption capability of the plasmonic Au-BiVO<sub>4</sub> design has been coupled with a WOC, called CoFe-PBA, to maximize the PEC-

WS performance of BiVO<sub>4</sub>. As a result of this improvement, a near an order of magnitude improvement is observed in Au-BiVO<sub>4</sub>/[CoFe], compared with that of bare BiVO<sub>4</sub>. A maximum of 43% above-band-gap IPCE and 1800 μA cm<sup>-2</sup> (at 1.23 V vs. RHE). Moreover, the <5% IPCE of sub-band-gap photons proves the fact that this structure benefits from the hot electron injection of plasmonic gold. This study, which presents one of the first examples of a plasmonic-enhanced photoelectrode coupled with a WOC assembly, indicates that unifying the strengths of WOCs and plasmonic structures can be a viable approach to increase the performance of photoelectrodes in the visible region. The large-scale compatible synthesis route for the plasmonic and WOC components has no material restrictions and can be extended into other efficient metal-semiconductor heterostructures.

## Experimental Section

### Chemicals and materials

The chemicals were used as received without further purification. Bismuth(III) nitrate pentahydrate (Bi(NO<sub>3</sub>)<sub>3</sub>·5H<sub>2</sub>O, Sigma-Aldrich, 99.99%), *p*-benzoquinone (C<sub>6</sub>H<sub>4</sub>(=O)<sub>2</sub>, Sigma-Aldrich, ≥98%), vanadyl acetylacetonate (OV(C<sub>5</sub>H<sub>7</sub>O<sub>2</sub>)<sub>2</sub>, Sigma-Aldrich, 98%) were used for nanoporous BiVO<sub>4</sub> synthesis on FTO-coated glass (2 mm thick, 7 Ω/sq, Solaronix). Potassium hexacyanoferrate(III) (K<sub>3</sub>[Fe(CN)<sub>6</sub>], 99%, Sigma-Aldrich), cobalt nitride hexahydrate CoNO<sub>3</sub>·6H<sub>2</sub>O (Fluka, ≥98%), and Millipore deionized water (resistivity: 18 mΩ cm) was used for the Prussian blue coating.

### Synthesis of BiVO<sub>4</sub> photoanode

Nanoporous BiVO<sub>4</sub> photoanodes were prepared by a modified method reported by Choi and co-workers.<sup>[90]</sup> Nanoporous BiVO<sub>4</sub> photoanodes were prepared by the electrodeposition of bismuth oxyiodide (BiOI) film followed by dipping of vanadium solution and heat treatment. To prepare a BiOI electrodeposition solution, sodium iodide (NaI, 1.49 g) was dissolved in DI water (25 mL) and the pH of the solution was adjusted to 1.8 by using nitric acid (HNO<sub>3</sub>). Then, bismuth(III) nitrate pentahydrate (Bi(NO<sub>3</sub>)<sub>3</sub>·5H<sub>2</sub>O, 480 mg) was added to the NaI solution and stirred for 30 min. *p*-Benzoquinone (240 mg) was dissolved in dimethyl sulfoxide (DMSO, 10 mL), and stirred for 15 min. The stirred solution was then added to the BiOI solution. The BiOI film was electrodeposited on FTO-coated glass under -0.1 V bias vs. Ag/AgCl electrode for 2 min. Electrodeposited films were washed with DI water to remove the remaining solution and dried in air. Then, 1 μL of a 0.4 M solution of vanadyl acetylacetonate (VO(acac)<sub>2</sub>) in ethanol was dropped onto a 1 cm<sup>2</sup> area of the BiOI films, followed by annealing at 450 °C for 2 h (ramping rate: 2 °C min<sup>-1</sup>). Finally, the samples were soaked in 1 M NaOH solution and stirred gently for 30 min to remove the extra vanadium oxide from the electrode surfaces.

### Cobalt hexacyanoferrate-modified BiVO<sub>4</sub>, BiVO<sub>4</sub>/[CoFe]

The Prussian blue coatings were prepared according to the previously reported procedure with slight modifications.<sup>[85]</sup> In detail, BiVO<sub>4</sub> electrodes were soaked in [K<sub>3</sub>Fe(CN)<sub>6</sub>] (0.02 M) in Milli-Q water solution for 1 min at room temperature. The samples were then rinsed with water to remove the non-adsorbed Fe<sup>2+</sup> ions.

Once the substrate was completely dried, the electrode was immersed in Co(NO<sub>3</sub>)<sub>2</sub>·6H<sub>2</sub>O solution (0.04 M) for a minute. Then, the electrode surface was washed with distilled water to remove the excess Co<sup>2+</sup> ions over the film. This process was repeated at least two times to ensure the full coverage of the Prussian blue analog. Finally, the BiVO<sub>4</sub>/[CoFe] electrode was left to dry at room temperature.

### Synthesis of Au-capped Prussian blue-modified BiVO<sub>4</sub>, Au-BiVO<sub>4</sub>/[CoFe]

Later, by using the angled deposition technique, 20 nm gold was evaporated onto the BiVO<sub>4</sub>/[CoFe] to form an Au-capped BiVO<sub>4</sub> nanoporous photoanode.

### Materials characterization

The morphological characteristics of the synthesized photoanode materials were performed by using a scanning electron microscope (SEM, FEI—Quanta 200 FEG) operated at 10 kV and a focused ion beam (FIB) operated at 15 kV. X-ray photoelectron spectroscopy (XPS, Thermo Scientific K-Alpha, AL K-Alpha radiation,  $h\nu = 1486.6$  eV) measurements were performed in survey mode by operating a flood gun to prevent surface charging with the pass energy and a step size set to 30 eV and 0.1 eV, respectively. Peak position correction was calibrated by referencing the C1s peak position (284.8 eV) and shifting other peaks in the spectrum accordingly. For the optical characterization of the electrode, UV/Vis spectra of the films were collected (Shimadzu UV-3600 UV/Vis/NIR Spectrophotometer) in diffuse reflection mode and converted to absorption spectra by the Kubelka–Munk transformation. GIXRD patterns were collected by using a Bruker D8 Advance X-ray Diffractometer and the measurements were done at a grazing incidence angle (1 degree). Raman spectroscopy investigations were performed by using a Renishaw Invia Raman Microscope using 532 nm excitation laser sources.

### Photoelectrochemical measurements

(Photo)electrochemical measurements were performed by using a Gamry Instruments Interface 1000 Potentiostat/Galvanostat in a standard three-electrode electrochemical cell configuration using a Pt mesh counter electrode, Ag/AgCl (saturated KCl) reference electrode, and BiVO<sub>4</sub> photoanodes with an exposed area of 1 cm<sup>2</sup> as the working electrodes. All of the calculations were based on the geometric surface area, unless specified otherwise. The measurements on photoanodes have been performed in phosphate-buffered saline (0.5 M Na<sub>2</sub>SO<sub>4</sub> in 0.1 M PBS, pH 7 at 25 °C) and, prior to each measurement, the electrolyte solution was saturated with N<sub>2</sub> gas (99.999% purity) for 30 min to remove the dissolved O<sub>2</sub> gas. The solar light simulator (Sciencetech, Model SLB-300B, 300 W Xe lamp, AM 1.5 global filter) was calibrated to 1 sun (100 mW cm<sup>-2</sup>) by using a thermopile optical detector (Newport, Model 818P-010-12). The current density–voltage ( $j$ - $V$ ) curves were measured on photoanodes in 0.1 M PBS under dark and light conditions with a scanning rate of 50 mV s<sup>-1</sup> between -0.4 and 1 V (vs. Ag/AgCl) by the linear sweep voltammetry (LSV) measurements. The potentials were converted to V vs. RHE (reversible hydrogen electrode) by using the Nernst equation:

$$V_{\text{RHE}} = V_{\text{Ag/AgCl}} (\text{V}) + 0.059 \times \text{pH} + V_{\text{Ag/AgCl}}^{\circ} (\text{V})$$

where  $V_{\text{RHE}}$  is the applied potential versus RHE;  $V_{\text{Ag/AgCl}}$  (V) is the applied potential versus Ag/AgCl reference electrode;  $V^{\circ}_{\text{Ag/AgCl}}$  (V) is the standard potential of the reference electrode ( $0.197 V_{\text{RHE}}$ ). Transient photocurrent measurements by the chronoamperometry (CA) technique, electrochemical impedance spectroscopy (EIS) under light conditions, and open-circuit voltage decay (OCVD) were also conducted. EIS spectra were recorded in the frequency range from 100 kHz to 0.1 Hz at a bias of 1.23 V vs. RHE with an alternating current (AC) voltage of 10 mV. For incident photon-to-current conversion efficiency (IPCE) measurements, light from the xenon lamp was dispersed by a monochromator and the photocurrent was recorded at a constant bias (1.23 V vs. RHE) with a spectral step of 10 nm. This light is entered into a monochromator (Oriol 1/8 m cornerstone, 1200 lines  $\text{mm}^{-1}$  grating) and the output of the monochromator is illuminated onto the photoanode.

## Acknowledgements

This work was supported by the Scientific and Technological Research Council of Turkey (TUBITAK), grant number 215Z249. This work was supported by the project DPT-HAMIT as well as TUBITAK under the project nos. 113E331, 114E374, and 115F560. One of the authors (E.O.) also acknowledges partial support from the Turkish Academy of Sciences. F.K. thanks TÜBA-GEBİP for young investigator award and BAGEP for young scientist award.

## Conflict of interest

The authors declare no conflict of interest.

**Keywords:** cyanide chemistry • hot electrons • photoelectrochemical water splitting • plasmonics • Prussian blue

- [1] T. G. U. Ghobadi, A. Ghobadi, E. Ozbay, F. Karadas, *ChemPhotoChem* **2018**, *2*, 161.
- [2] W. Hou, S. B. Cronin, *Adv. Funct. Mater.* **2013**, *23*, 1612.
- [3] A. M. Brown, R. Sundararaman, P. Narang, W. A. Goddard, H. A. Atwater, *ACS Nano* **2016**, *10*, 957.
- [4] G. Liu, K. Du, J. Xu, G. Chen, M. Gu, C. Yang, K. Wang, H. Jakobsen, *J. Mater. Chem. A* **2017**, *5*, 4233.
- [5] A. Ghobadi, T. G. Ulusoy Ghobadi, F. Karadas, E. Ozbay, *Adv. Opt. Mater.* **2019**, *7*, 1900028.
- [6] Y. H. Chiu, T. F. M. Chang, C. Y. Chen, M. Sone, Y. J. Hsu, *Catalysts* **2019**, *9*, 430.
- [7] Y. H. Chiu, T. H. Lai, M. Y. Kuo, P. Y. Hsieh, Y. J. Hsu, *APL Mater.* **2019**, *7*, 080901.
- [8] Z. Zhan, J. An, H. Zhang, R. V. Hansen, L. Zheng, *ACS Appl. Mater. Interfaces* **2014**, *6*, 1139.
- [9] Z. Liu, W. Hou, P. Pavaskar, M. Aykol, S. B. Cronin, *Nano Lett.* **2011**, *11*, 1111.
- [10] Y. C. Pu, G. Wang, K. Der Chang, Y. Ling, Y. K. Lin, B. C. Fitzmorris, C. M. Liu, X. Lu, Y. Tong, J. Z. Zhang, Y. J. Hsu, Y. Li, *Nano Lett.* **2013**, *13*, 3817.
- [11] P. A. Desario, J. J. Pietron, D. E. Devantier, T. H. Brintlinger, R. M. Stroud, D. R. Rolison, *Nanoscale* **2013**, *5*, 8073.
- [12] Z. Zhang, L. Zhang, M. N. Hedhili, H. Zhang, P. Wang, *Nano Lett.* **2013**, *13*, 14.
- [13] T. G. Ulusoy Ghobadi, A. Ghobadi, F. Karadas, E. Ozbay, *Int. J. Hydrogen Energy* **2020**, *45*, 1521.
- [14] A. Naldoni, F. Riboni, M. Marelli, F. Bossola, G. Ulisse, A. Di Carlo, I. Piš, S. Nappini, M. Malvestuto, M. V. Dozzi, R. Psaro, E. Selli, V. Dal Santo, *Catal. Sci. Technol.* **2016**, *6*, 3220.
- [15] S. Farsinezhad, H. Sharma, K. Shankar, *Phys. Chem. Chem. Phys.* **2015**, *17*, 29723.
- [16] H. C. Ho, K. Chen, T. Nagao, C. H. Hsueh, *J. Phys. Chem. C* **2019**, *123*, 21103.
- [17] N. Wu, *Nanoscale* **2018**, *10*, 2679.
- [18] M. Valenti, M. P. Jonsson, G. Biskos, A. Schmidt-Ott, W. A. Smith, *J. Mater. Chem. A* **2016**, *4*, 17891.
- [19] D. Hu, P. Diao, D. Xu, Q. Wu, *Nano Res.* **2016**, *9*, 1735.
- [20] P. Subramanyam, B. Meena, G. N. Sinha, M. Deepa, C. Subrahmanyam, *Int. J. Hydrogen Energy* **2020**, *45*, 7706–7711.
- [21] P. Mishra, S. Patnaik, K. Parida, *Catal. Sci. Technol.* **2019**, *9*, 916.
- [22] A. J. Cheah, W. S. Chiu, P. S. Khiew, H. Nakajima, T. Saisopa, P. Songsiriritthigul, S. Radiman, M. A. A. Hamid, *Catal. Sci. Technol.* **2015**, *5*, 4133.
- [23] K. C. Hung, Y. H. Lai, T. W. Lin, *Catal. Sci. Technol.* **2016**, *6*, 4020.
- [24] J. M. Li, H. Y. Cheng, Y. H. Chiu, Y. J. Hsu, *Nanoscale* **2016**, *8*, 15720.
- [25] Y. L. Huang, W. S. Chang, C. Van Nguyen, H. J. Liu, K. A. Tsai, J. W. Chen, H. H. Kuo, W. Y. Tzeng, Y. C. Chen, C. L. Wu, C. W. Luo, Y. J. Hsu, Y. H. Chu, *Nanoscale* **2016**, *8*, 15795.
- [26] J. M. Li, C. W. Tsao, M. J. Fang, C. C. Chen, C. W. Liu, Y. J. Hsu, *ACS Appl. Nano Mater.* **2018**, *1*, 6843.
- [27] Y. H. Chiu, S. B. Naghadeh, S. A. Lindley, T. H. Lai, M. Y. Kuo, K. Der Chang, J. Z. Zhang, Y. J. Hsu, *Nano Energy* **2019**, *62*, 289.
- [28] K. H. Chen, Y. C. Pu, K. Der Chang, Y. F. Liang, C. M. Liu, J. W. Yeh, H. C. Shih, Y. J. Hsu, *J. Phys. Chem. C* **2012**, *116*, 19039.
- [29] A. Ghobadi, T. G. Ulusoy Ghobadi, F. Karadas, E. Ozbay, *Adv. Opt. Mater.* **2019**, *7*, 1900028.
- [30] C. N. Van, W. S. Chang, J. W. Chen, K. A. Tsai, W. Y. Tzeng, Y. C. Lin, H. H. Kuo, H. J. Liu, K. Der Chang, W. C. Chou, C. L. Wu, Y. C. Chen, C. W. Luo, Y. J. Hsu, Y. H. Chu, *Nano Energy* **2015**, *15*, 625.
- [31] Z. Zheng, W. Xie, B. Huang, Y. Dai, *Chem. Eur. J.* **2018**, *24*, 18322.
- [32] L. Wang, X. Zhou, N. T. Nguyen, P. Schmuki, *ChemSusChem* **2015**, *8*, 618.
- [33] H. Bai, P. Guan, K. Qu, W. Fan, F. Wang, D. Xu, J. Ding, W. Shi, *Int. J. Hydrogen Energy* **2019**, *44*, 28184.
- [34] S. Kim, Y. Yu, S. Y. Jeong, M. G. Lee, H. W. Jeong, Y. M. Kwon, J. M. Baik, H. Park, H. W. Jang, S. Lee, *Catal. Sci. Technol.* **2018**, *8*, 3759.
- [35] B. Chen, Z. Zhang, M. Baek, S. Kim, W. Kim, K. Yong, *Appl. Catal. B* **2018**, *237*, 763.
- [36] L. Wang, H. Hu, N. T. Nguyen, Y. Zhang, P. Schmuki, Y. Bi, *Nano Energy* **2017**, *35*, 171.
- [37] Z. Xu, Z. Fan, Z. Shi, M. Li, J. Feng, L. Pei, C. Zhou, J. Zhou, L. Yang, W. Li, G. Xu, S. Yan, Z. Zou, *ChemSusChem* **2018**, *11*, 237.
- [38] G. C. Li, Q. Zhang, S. A. Maier, D. Lei, *Nanophotonics* **2018**, *7*, 1865.
- [39] Q. Pan, C. Zhang, Y. Xiong, Q. Mi, D. Li, L. Zou, Q. Huang, Z. Zou, H. Yang, *ACS Sustainable Chem. Eng.* **2018**, *6*, 6378.
- [40] S. Y. Jeong, H. M. Shin, Y. R. Jo, Y. J. Kim, S. Kim, W. J. Lee, G. J. Lee, J. Song, B. J. Moon, S. Seo, H. An, S. H. Lee, Y. M. Song, B. J. Kim, M. H. Yoon, S. Lee, *J. Phys. Chem. C* **2018**, *122*, 7088.
- [41] A. Kushwaha, M. Aslam, *RSC Adv.* **2014**, *4*, 20955.
- [42] H. Kim, C. Choi, J. Khamwannah, S. Young Noh, Y. Zhang, T. Y. Seong, S. Jin, *J. Renewable Sustainable Energy* **2013**, *5*, 053104.
- [43] D. U. Yildirim, A. Ghobadi, M. C. Soydan, O. Atesal, A. Toprak, M. D. Caliskan, E. Ozbay, *ACS Photonics* **2019**, *6*, 1812.
- [44] M. C. Soydan, A. Ghobadi, D. U. Yildirim, E. S. Duman, A. Bek, V. B. Erturk, E. Ozbay, *Adv. Opt. Mater.* **2019**, *7*, 1901203.
- [45] T. G. Ulusoy Ghobadi, E. Akhuseyin Yildiz, M. Buyuktemiz, S. Sadigh Akbari, D. Topkaya, Ü. İsci, Y. Dede, H. G. Yaglioglu, F. Karadas, *Angew. Chem. Int. Ed.* **2018**, *57*, 17173; *Angew. Chem.* **2018**, *130*, 17419.
- [46] T. G. Ulusoy Ghobadi, A. Ghobadi, M. Buyuktemiz, E. A. Yildiz, D. B. Yildiz, H. G. Yaglioglu, Y. Dede, E. Ozbay, F. Karadas, *Angew. Chem. Int. Ed.* **2020**, *59*, 4082; *Angew. Chem.* **2020**, *132*, 4111.
- [47] A. Barranco, A. Borras, A. R. Gonzalez-Elipe, A. Palmero, *Prog. Mater. Sci.* **2016**, *76*, 59.
- [48] J. Yu, A. Kudo, *Adv. Funct. Mater.* **2006**, *16*, 2163.
- [49] R. L. Frost, D. A. Henry, M. L. Weier, W. Martens, *J. Raman Spectrosc.* **2006**, *37*, 722.
- [50] A. K. Bhattacharya, K. K. Mallick, A. Hartridge, *Mater. Lett.* **1997**, *30*, 7.
- [51] M. Guo, Y. Wang, Q. He, W. Wang, W. Wang, Z. Fu, H. Wang, *RSC Adv.* **2015**, *5*, 58633.
- [52] C. Regmi, D. Dhakal, S. W. Lee, *Nanotechnology* **2018**, *29*, 064001.
- [53] S. Bao, Q. Wu, S. Chang, B. Tian, J. Zhang, *Catal. Sci. Technol.* **2017**, *7*, 124.

- [54] J. Qi, D. Kong, D. Liu, L. Pan, Y. Chen, X. Zhang, J. J. Zou, *RSC Adv.* **2019**, *9*, 15629.
- [55] N. Kruse, S. Chenakin, *Appl. Catal. A* **2011**, *391*, 367.
- [56] S. Nayak, K. M. Parida, *ACS Omega* **2018**, *3*, 7324.
- [57] F. Su, T. Wang, R. Lv, J. Zhang, P. Zhang, J. Lu, J. Gong, *Nanoscale* **2013**, *5*, 9001.
- [58] Y. Shiraishi, N. Yasumoto, J. Imai, H. Sakamoto, S. Tanaka, S. Ichikawa, B. Ohtani, T. Hirai, *Nanoscale* **2017**, *9*, 8349.
- [59] A. Ghobadi, T. G. U. Ghobadi, F. Karadas, E. Ozbay, *Sci. Rep.* **2018**, *8*, 16322.
- [60] X. Zhang, J. Qin, Y. Xue, P. Yu, B. Zhang, L. Wang, R. Liu, *Sci. Rep.* **2014**, *4*, 4.
- [61] J. C. Dupin, D. Gonbeau, P. Vinatier, A. Levasseur, *Phys. Chem. Chem. Phys.* **2000**, *2*, 1319.
- [62] S. Wang, P. Chen, Y. Bai, J. H. Yun, G. Liu, L. Wang, *Adv. Mater.* **2018**, *30*, 1802883.
- [63] F. Liu, L. Lu, P. Xiao, H. He, L. Qiao, Y. Zhang, *Bull. Korean Chem. Soc.* **2012**, *33*, 2255.
- [64] M. Zhang, C. Shao, X. Li, P. Zhang, Y. Sun, C. Su, X. Zhang, J. Ren, Y. Liu, *Nanoscale* **2012**, *4*, 7501.
- [65] M. Barzgar Vishlaghi, A. Kahraman, S. Kaya, *J. Phys. Chem. C* **2020**, *124*, 1337.
- [66] T. Li, J. He, B. Peña, C. P. Berlinguette, *Angew. Chem. Int. Ed.* **2016**, *55*, 1769; *Angew. Chem.* **2016**, *128*, 1801.
- [67] H. L. Tan, A. Suyanto, A. T. De Denko, W. H. Saputera, R. Amal, F. E. Osterloh, Y. H. Ng, *Part. Part. Syst. Character.* **2017**, *34*, 1600290.
- [68] A. Ghobadi, H. I. Yavuz, T. G. Ulusoy, K. C. Icli, M. Ozenbas, A. K. Okyay, *Electrochim. Acta* **2015**, *157*, 23.
- [69] T. Wei, Y. N. Zhu, Z. Gu, X. An, L. Liu, Y. Wu, H. Liu, J. Tang, J. Qu, *Nano Energy* **2018**, *51*, 764.
- [70] Q. T. Liu, D. Y. Liu, J. M. Li, Y. B. Kuang, *Front. Phys.* **2019**, *14*, 53403.
- [71] F. S. Hegner, D. Forrer, J. R. Galán-Mascarós, N. López, A. Selloni, *J. Phys. Chem. Lett.* **2019**, *10*, 6672.
- [72] S. Selim, E. Pastor, M. García-Tecedor, M. R. Morris, L. Francàs, M. Sachs, B. Moss, S. Corby, C. A. Mesa, S. Gimenez, A. Kafizas, A. A. Bakulin, J. R. Durrant, *J. Am. Chem. Soc.* **2019**, *141*, 18791.
- [73] Z. Wang, X. Mao, P. Chen, M. Xiao, S. A. Monny, S. Wang, M. Konarova, A. Du, L. Wang, *Angew. Chem. Int. Ed.* **2019**, *58*, 1030; *Angew. Chem.* **2019**, *131*, 1042.
- [74] W. J. Yin, S. H. Wei, M. M. Al-Jassim, J. Turner, Y. Yan, *Phys. Rev. B* **2011**, *83*, 155102.
- [75] G. Wang, Y. Ling, X. Lu, F. Qian, Y. Tong, J. Z. Zhang, V. Lordi, C. Rocha Leao, Y. Li, *J. Phys. Chem. C* **2013**, *117*, 10957.
- [76] L. Liu, P. Li, B. Adisak, S. Ouyang, N. Umezawa, J. Ye, R. Kodiyath, T. Tanabe, G. V. Ramesh, S. Ueda, H. Abe, *J. Mater. Chem. A* **2014**, *2*, 9875.
- [77] T. G. Ulusoy Ghobadi, A. Ghobadi, T. Okyay, K. Topalli, A. K. Okyay, *RSC Adv.* **2016**, *6*, 112520.
- [78] J. K. Cooper, S. Gul, F. M. Toma, L. Chen, P. A. Glans, J. Guo, J. W. Ager, J. Yano, I. D. Sharp, *Chem. Mater.* **2014**, *26*, 5365.
- [79] L. Mascaretti, A. Dutta, Š. Kment, V. M. Shalaev, A. Boltasseva, R. Zbořil, A. Naldoni, *Adv. Mater.* **2019**, *31*, 1805513.
- [80] M. Haro, R. Abargues, I. Herraiz-Cardona, J. Martínez-Pastor, S. Giménez, *Electrochim. Acta* **2014**, *144*, 64.
- [81] X. An, T. Li, B. Wen, J. Tang, Z. Hu, L. M. Liu, J. Qu, C. P. Huang, H. Liu, *Adv. Energy Mater.* **2016**, *6*, 1502268.
- [82] Y. H. Lu, W. H. Lin, C. Y. Yang, Y. H. Chiu, Y. C. Pu, M. H. Lee, Y. C. Tseng, Y. J. Hsu, *Nanoscale* **2014**, *6*, 8796.
- [83] Y. H. Chiu, T. H. Lai, C. Y. Chen, P. Y. Hsieh, K. Ozasa, M. Niinomi, K. Okada, T. F. M. Chang, N. Matsushita, M. Sone, Y. J. Hsu, *ACS Appl. Mater. Interfaces* **2018**, *10*, 22997.
- [84] In Lumerical Solut. Inc. <http://www.lumerical.com/Tcad-Products/Fdtd/>, n.d..
- [85] F. S. Hegner, I. Herraiz-Cardona, D. Cardenas-Morcoso, N. López, J. R. Galán-Mascarós, S. Gimenez, *ACS Appl. Mater. Interfaces* **2017**, *9*, 37671.
- [86] B. Moss, F. S. Hegner, S. Corby, S. Selim, L. Francàs, N. López, S. Giménez, J. R. Galán-Mascarós, J. R. Durrant, *ACS Energy Lett.* **2019**, *4*, 337.
- [87] J. H. Kim, J. S. Lee, *Adv. Mater.* **2019**, *31*, 1.
- [88] H. S. Han, S. Shin, D. H. Kim, I. J. Park, J. S. Kim, P. S. Huang, J. K. Lee, I. S. Cho, X. Zheng, *Energy Environ. Sci.* **2018**, *11*, 1299.
- [89] Y. Pihosh, I. Turkevych, K. Mawatari, J. Uemura, Y. Kazoe, S. Kosar, K. Makita, T. Sugaya, T. Matsui, D. Fujita, M. Tosa, M. Kondo, T. Kitamori, *Sci. Rep.* **2015**, *5*, 11141.
- [90] T. W. Kim, K.-S. Choi, *Science* **2014**, *343*, 990.

---

Manuscript received: February 4, 2020

Revised manuscript received: March 6, 2020

Accepted manuscript online: March 11, 2020

Version of record online: April 16, 2020